Journal of Power Sources 182 (2008) 175–187

Contents lists available at ScienceDirect

Journal of Power Sources

journal homepage: www.elsevier.com/locate/jpowsour

Degradation effects in polymer electrolyte membrane fuel cell stacks by sub-zero operation—An in situ and ex situ analysis

R. Alink, D. Gerteisen*, M. Oszcipok

Fraunhofer Institute for Solar Energy Systems, Freiburg, Germany

ARTICLE INFO

Article history:
Received 8 October 2007
Received in revised form 17 March 2008
Accepted 21 March 2008
Available online 3 April 2008

Keywords:
PEMFC
Freeze–thaw cycling
Cold start
Outdoor application
Degradation

ABSTRACT

The effect of low temperatures down to −40 °C on the performance and component properties of a polymer electrolyte membrane (PEM) fuel cell stack was investigated.

By analyzing the temperature-dependent high-frequency resistance, the mechanism of ice formation within the stack was investigated during freeze/thaw (F/T) cycling while the stack was not operating and during a cold start-up. A step-like change in conductivity at 0 °C indicates that the membranes are dehydrated at sub-zero temperatures due to a change in capillary pressure at the interface membrane/catalyst.

Furthermore, it was found that the stack shows little degradation when it is dried out before cooling down. Freezing in a wet state and additional cold start-ups resulted in performance degradation which was mainly attributed to changes in wetting properties. Ex situ environmental scanning electron microscope (ESEM) investigations showed distinct damage and increasing porosity of the electrode in the wet frozen stack, which was most likely the reason for the change in wetting properties. Inductively coupled plasma (ICP) mass spectroscopy showed distinct concentrations of platinum in the exhaust gas of the dry cycled stack, but no additional platinum was found when the stack was cycled in a wet state.

Additional ex situ F/T investigations of gas diffusion layers (GDLs) and membrane electrode assemblies (MEAs) within an ESEM confirmed the results, found by in situ investigations of the fuel cell stacks. Serious detachment of electrode material was found without the compressive force applied to an assembly.

1. Introduction

The durability of fuel cells under various ambient conditions is an important issue for successful commercialisation.

Until now, little work has been done to understand the degradation mechanisms in PEM fuel cell stacks under sub-zero conditions and considering the importance of the topic for PEM fuel cells, few articles have been published.

Pesaran et al. divide methods for cold start-up or storage of PEM fuel cells under freezing conditions into so-called keep-warm methods and thaw/heating methods [1]. Thaw/heating methods include passive fuel cell start-up and heating by catalytic burners as well as electric heating methods to make different outdoor applications for PEM fuel cells [2]. However, thaw/heating methods can lead to degradation effects at low temperatures.

McDonald et al. did not observe degradation of mechanical properties during 385 freeze/thaw (F/T) cycles (freezing and thawing in the inoperative state) of pure Nafion© and membrane electrode assemblies (MEAs) in a dry state [3].

Water is produced during the operation of a fuel cell. In PEMFCs, water within the cell is necessary to ensure high protonic conductivity of the polymer electrolyte membrane. During normal operation, the generated waste heat is sufficient to keep the water within the cell above the freezing point, even at ambient temperatures significantly below 0 °C. However, when fuel cells are switched off under sub-zero conditions, the volume expansion by ice formation within the cell can lead to structural damage. In order to ensure good gas diffusivity and to extend the electrochemically active surface area, the materials of the gas diffusion layers (GDLs), micro-porous layer (MPL) and electrodes are highly porous. If water freezes within these media, volume expansion can lead to cracks in their structure [4] and a change in the pore size distribution of the electrodes [5–7]. Furthermore, carbon fibre breakage, loss of hydrophobicity [8,9] in GDLs as well as damage to the MPL [10] can occur. Besides the damage by ice expansion Kim and Mench suggest that frost heave damage as known from damage in road surfaces exposed under freezing conditions can be a further degradation mechanism in PEM fuel cells [11].

The physical state of water within the membrane seems to be a key issue in membrane degradation under freezing conditions. Due to the high capillary pressure in small pores, the freezing point of water within the membrane can fall below 0 °C. In a Nafion©

* Corresponding author. Tel.: +49 761 4588 5205; fax: +49 761 4588 9205.
E-mail address: dietmar.gerteisen@ise.fraunhofer.de (D. Gerteisen).

0378-7753/$ – see front matter © 2008 Elsevier B.V. All rights reserved.
doi:10.1016/j.jpowsour.2008.03.074

Nomenclature

A_i	detected electrode surface area in MEA cross-section
A_{new}	detected electrode surface area in MEA cross-sections of new MEA
D_n	degradation rate after n sub-zero exposures (mV per sub-zero exposure)
$\tilde{E}$	perturbed cell potential (V)
E_A	activation energy (kJ mol^{-1})
ΔE_A	difference of activation energies between high and low temperatures (kJ mol^{-1})
ECSA	electrochemical surface area
EDX	energy dispersive X-ray spectroscopy
EIS	electrochemical impedance spectroscopy
ESEM	environmental scanning electron microscope
F/T	freeze–thaw
GDL	gas diffusion layer
HFR	high-frequency resistance (Ω cm^2)
$\tilde{i}$	perturbed current density (A cm^{-2})
i_{st}	steady-state current density (A cm^{-2})
ICP-MS	inductively coupled plasma mass spectroscopy
MEA	membrane electrode assembly
MPL	micro-porous layer
OCV	open circuit voltage (V)
$R_{D,T}$	Tafel charge-transfer resistance (V)
RH	relative humidity
RSTD	relative standard deviation
stackD	stack, frozen in a "dry" state
stackR	reference stack
stackW	stack, frozen in a "wet" state
stackD$_{F/T}$	stackD during freeze–thaw cycling
stackW$_{CS}$	stackW during cold start-ups
stackW$_{F/T}$	stackW during freeze–thaw cycling
sub-zero exposure	freeze–thaw cycle or cold start-up
SEM	scanning electron microscopy
STD	standard deviation
ΔX_e	decrease of detected electrode surface area in MEA cross-sections (%)
Z	impedance (Ω cm^2)
Z_t	Tafel impedance (V)

Greek letters

δ	thickness of membrane (cm)
λ	H_2O per charged site
σ	conductivity (S cm^{-1})

membrane, besides free and loosely bound freezable water, non-freezing water can be present which is still moveable even at −20 °C [5].

Some aspects of degradation caused by F/T cycling are discussed controversially in literature.

For the membrane/electrode interface, Kim et al., Cho et al. and Wang et al. reported delamination of the electrodes from the membrane due to F/T cycling [11–13,7] while Hou et al. did not find any indication for delamination of catalyst layers [5]. Performance degradation due to F/T cycling, especially at high current densities, was found in Refs. [12,13,5]. Cho et al. reports a performance degradation rate of 2.8% per F/T cycle at 600 mV for a single cell after four F/T cycles [12,13]. However, Mukundan et al. did not find any performance degradation after 100 F/T cycles in a single cell using E-TEK double-sided wet-proof carbon cloth [8]. Degradation in PEM fuel cells seems to be highly dependent on the cell components.

Purging with reactant gases seems to be a promising approach to prevent degradation of PEMFCs caused by F/T cycling. Such purging procedures are applied before switching off in order to remove residual water from the porous media [14–16]. In Ref. [5] changes in performance, high-frequency resistance (HFR), electrochemical surface area (ECSA) or charge-transfer resistance and electrode delamination were not found, if the cell had been dried out by reactant gases to a relative humidity (RH) of 16.6% or lower.

When a fuel cell is started at sub-zero temperatures, freezing product water blocks the gas diffusion pathway to the electrodes and can also lead to structural damage. If heat production is sufficient to reach cell temperatures above 0 °C before the cell voltage breaks down, a passive cold start is possible, but degradation can still occur [6,17].

In this paper, we present the results of a comprehensive examination of the influence of 120 F/T cycles in a dry state and 62 F/T cycles in a wet state on cell components and cell performance of a portable PEM fuel cell stack. Additionally a series of nine isothermal cold start-up experiments was conducted, which represents the worst-case scenario for a passive cold start-up strategy.

The experimental study started with an investigation of the HFR of the PEMFC stacks during thermal cycling (Section 3.1). This provided new fundamental insights on pressure and membrane water saturation during the phase transition of water in the catalyst layer.

Between the F/T cycles and cold start-ups, the stacks were characterized by measuring polarisation curves and dynamic load changes (Section 3.2) and conducting electrochemical impedance spectroscopy (EIS) (Section 3.3). Environmental scanning electron microscope (ESEM) and energy dispersive X-ray spectroscopy (EDX) analyses of fuel cell components and inductively coupled plasma (ICP) mass spectroscopy of product water (Section 3.4) as well as contact angle measurements (Section 3.5) of the GDL were conducted ex situ. The single cells were characterized separately to determine the influence of inhomogeneous conditions within the stack.

2. Experimental

2.1. Stack set-up

Two PEM fuel cell stacks were set up to investigate the impact of low-temperature cycling on either a stack which was dried out before freezing (stackD) and a stack which was frozen in a wet state (stackW) directly after normal operation.

The fuel cell stacks consisted of six cells with an active area of 30 cm^2 and graphite compound bipolar plates with double serpentine flow channels as described in Ref. [2]. Commercial MEAs from the same supplier and the same type with a platinum loading of 0.4 mg cm^{-2} in stackD and 0.3 mg cm^{-2} in stackW in combination with Toray TGP-H-060 GDLs were used. Viton gaskets served as sealing and copper plates as current collectors. To improve heat removal, cooling fins were integrated into the aluminum end-plates.

2.2. Climatic chamber test bench

A test bench with a climatic chamber (Vötsch VC 4034) was used for testing fuel cell systems under realistic conditions. It was then possible to investigate the operation of fuel cell systems and fuel cell stacks under environmental conditions in a range between −40 °C and 100 °C, and 10% and 98% RH. All the main components were controlled by LabView© and all signals were monitored via a data logger and PCI measuring card. Gases would be supplied to the fuel cell in a humidified or dry state. The electronic load (Zentro EL)

could handle a maximum current of 125 A. High-frequency resistance was measured with a high frequency response analyzer (HP 4328A) at 1 kHz.

Additionally equipment to measure electrochemical impedance spectroscopy was connected to the climatic chamber test bench (Princeton 263A, Kepco BOP 20-20M, PerkinElmer 5210).

2.3. Freeze–thaw cycles and cold start-up experiments

In order to freeze stacks in a dry or a wet state, two different conditioning procedures were applied before the temperature was lowered.

The drying procedure for stackD had the following operational sequence:

First the stack was operated at 50 mA cm^{-2} for 10 min. After that, the average single-cell HFR was minimal at 140 mΩ cm^2. Next, the stack was dried with dry air (8.0 l min^{-1}) and dry hydrogen (3.5 l min^{-1}) until the HFR reached 281 mΩ cm^2. Then gases were set to a flow rate of 1.0/1.0 until the HFR reached 507 mΩ cm^2. Afterwards the gas flow rates were controlled to keep the HFR constant at a level of 507 mΩ cm^2 for 5 min. After completing this drying procedure, the stack was cooled down.

For the wet cycles of stackW the following conditioning procedure was applied:

After operating the stack at 50 mA cm^{-2} for 5 min, the stack was dried out with gas flow rates of 8.0 l min^{-1} (air)/3.5 l min^{-1} (H_2). When the stack HFR reached 225 mΩ cm^2, gases were controlled to stabilize the HFR for 5 min. In order to humidify the components and to ensure a constant amount of water within the stack at minimal HFR, it was again operated at 50 mA cm^{-2} for 5 min. By following this procedure, it was possible to achieve a very well-defined, reproducible wetting state in the stack.

During the F/T cycles, the electronic load and gases were switched off. The cooling/heating rate of the climatic chamber was between 1 °C min^{-1} and 2 °C min^{-1} and the stack was allowed to reach thermal equilibrium for 30 min at a low temperature.

Finally, after the "wet" F/T cycles, cold start-ups of stackW were conducted at a stack temperature of −40 °C. Before it was cooled down, the stack was conditioned in the same way as stackD before F/T cycling.

Each cold start-up was conducted with gas flow rates of 0.4/0.1 l min^{-1}. After the open circuit voltage (OCV) had stabilized, the stack was operated in the galvanostatic mode at 17 mA cm^{-2}. During this operation phase, the single-cell voltages declined because product water blocked the porous structure of the cathode catalyst layers. When the lowest single-cell voltage reached 0.15 V, operation was stopped automatically and the gases were turned off. These start-up experiments were repeated at intervals of 2 min until lowest single-cell OCV did not increase above 0.3 V anymore (typically after 15 times).

After the cycling procedure, both stacks had accumulated an operating time of about 90 h and were never operated at temperatures above 60 °C.

2.4. Performance and EIS measurements

Performance measurements of both stacks were conducted between several sub-zero experiments (F/T cycles or cold start-ups).

Steady-state performance was measured at four points after at least 5 min operation in the galvanostatic mode. Steady state was defined by the stack voltage variation, which had to be below 25 mV min^{-1}. In order to avoid performance losses due to accumulating water, the stack was purged briefly with reactant gases. By setting the climatic chamber to predefined temperatures, it was ensured that the stack temperatures remained below 60 °C during performance characterization.

For additional characterization of stackW, polarisation curves were recorded from 0 mA cm^{-2} to 500 mA cm^{-2} in steps of 16.5 mA cm^{-2} at an ambient temperature of 25 °C. The holding time per point was 30 s. Gas flow rates were set to a stoichiometry of 2 for air and 1.5 for hydrogen. Brief purging (1 s) with maximum gas flow rates (air: 8.0 l min^{-1}, H_2: 3.5 l min^{-1}) was conducted before each step to prevent water accumulation.

EIS were recorded in the potentiostatic mode at an average single-cell voltage of 0.84 V and a stack temperature of 27 °C. The perturbation amplitude was 10 mV per single cell. Twenty measurement points were recorded in the frequency range between 1 kHz and 0.1 Hz. Both the sense and the working electrode were connected to the cathode current collector while the counter electrode was connected to the anode current collector of the stack. The reference electrode could be connected to any of the bipolar plates to determine the impedance of single cells.

To prevent influence by residual water, the stacks were dried out in the same manner as before cooling down stackD, followed by 10 min of operation at a stack voltage of 5.04 V.

Depending on the stack current, gas flow rates were adjusted to a constant stoichiometry (air: 7.0/H_2: 5.0) in order to prevent both accumulation of bulk-water and drying of the stack. Due to this controlled gas flow rates, the stack HFR varied just little (Δ_{HFR} < 20 mΩ cm^{-2}) during each EIS characterization.

2.5. ESEM and ICP measurements

An ESEM (FEI Quanta 400) with integrated EDX (EDAX Genesis) was used for ex situ investigation of GDLs and MEAs. Samples from the middle of the GDLs and MEAs were cut and fixed on sample plugs for surface views. Cross-sections of MEAs were prepared by stacking samples of all cells and additionally a new MEA on top of each other. Each cell was separated from its neighbours by a plastic film. This MEA stack was assembled in a clamp and cut with a razor blade. By this method cross-sections of operated single-cell MEAs and new MEAs could be obtained very rapidly with good and comparable quality.

Product water from the anode and cathode exhaust gases was collected separately with a condenser during all in situ experiments. The product water was analyzed for its platinum content (isotopes 194 amu and 195 amu) using an inductively coupled plasma mass spectrometer (ICP-MS) (Agilent ICP-MS 7500ce).

2.6. Contact angle measurements

Contact angle measurements (Dataphysics OCA20) were conducted on GDLs of both stacks. The average contact angle of 10 water drops of 10 μl distilled water was used to determine changes in the surface wetting properties of each side of the GDLs.

2.7. Freeze–thaw investigations in ESEM with an integrated cryostatic sample holder

In combination with an integrated cryostatic sample holder (Emott HK102HT), sample temperatures from −45 °C to +200 °C as well as pressures from 10 Pa to 800 Pa could be adjusted in the ESEM. As the ESEM operates with a water vapour atmosphere, water can be condensed, frozen and sublimed on the samples. This was used to conduct comparative studies on structural changes by water freezing in MEAs and GDLs.

Samples of commercial MEAs with a platinum loading of 0.4 mg cm^{-2} and Toray TGP-H-060 GDLs were attached to the sample holder using carbon adhesive stickers before applying 10 F/T cycles.

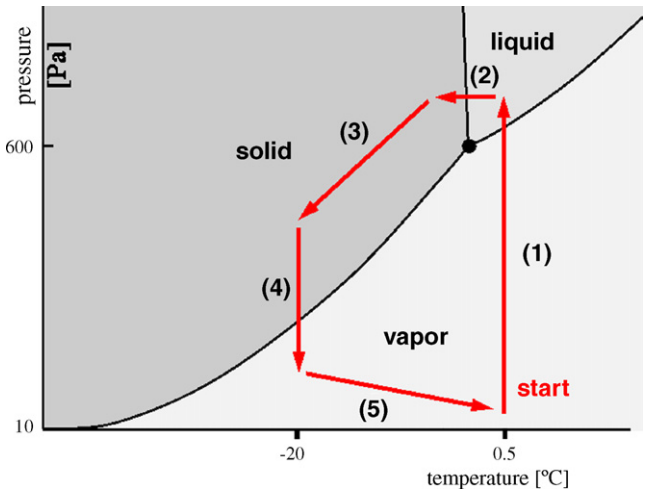

Fig. 1. Temperature and pressure during one F/T cycle in ESEM and phase diagram of water.

Every F/T cycle was started at 10 Pa and 0.5 °C (Fig. 1). Then the pressure was increased to 700 Pa (1) and as a result, water condensed on the sample. The temperature was held constant until the complete surface of the sample was covered with liquid water.

Subsequently, the cryostat was set to maximum cooling power (2). Due to water which was still condensing on samples/sample holder and the enthalpy of condensation, the temperature of the samples did not decrease below −4 °C until the pressure was lowered (3). Then water stopped condensing on the samples and the sample holder and the temperature was now thermodynamically free to drop down to −20 °C. In the following step, ice was sublimed by lowering the pressure (4), and the sample was heated up to 0.5 °C (5).

To avoid any effect of structural changes of the samples caused by the electron beam, different positions were used for visualizing ice/water formation and for comparative studies of structural changes.

3. Results and discussion

3.1. Temperature dependence of high-frequency resistance

Stack HFRs were recorded during all F/T cycles. Fig. 2 shows Arrhenius plots of the temperature-dependent specific conductivity σ:

$$\sigma = \frac{\delta}{\mathrm{HFR}}$$

(δ = thickness of membrane), while cooling down and heating up stackD (stack$D_{F/T}$) and stackW (stack$W_{F/T}$) during F/T cycling. Additionally, the Arrhenius plot of cooling before and heating after a cold start-up experiment with stackW is shown (stackW_{CS}). To demonstrate the good reproducibility of the experiments, two plots of each type are shown.

3.1.1. Hysteresis

Stack$W_{F/T}$ showed a strong hysteresis between freezing and warming-up. Stack$D_{F/T}$ does not show any hysteresis, so this effect is most likely attributed to water within the stack.

The cooling/heating rate of the climatic chamber was between 1 K min^{-1} and 2 K min^{-1}, so the hysteresis can be explained by temperature gradients evolving between the stack centre and the end-plates where the temperature was measured. During cooling, the temperature difference between the end-plates and the membranes increased due to additional excess heat corresponding to the crystallisation enthalpy of freezing water. The same effect occurs during heating when heat is consumed to melt ice. During the heating phase, the hysteresis already starts at −40 °C, indicating that the phase transition of water already occurs at such low temperatures. This lowering of the melting point can most likely be attributed to capillary pressure or increased pressure due to volume expansion at the phase transition of water.

A further effect can be superimposed on the phenomena mentioned above. When allying a temperature gradient across the membranes of single cells, drying effects of the membranes by water moving towards the colder side have already been observed by other groups [18]. A reason for this effect could be frost heave as described for road damage by Hermansson and Guthrie [19]. Some work has already been done to understand the physical fundamentals of this effect and its potential impact to the PEM fuel cell [20,11]. When exposed to sub-freezing conditions, water within porous structures begins to freeze at the colder side first. As the freezing progresses, the freezing front moves towards the warmer side. The decrease of the liquid water amount in the layer where ice forms first causes matric suction within the frozen zone and as a result, liquid water moves from the non-frozen region to the frozen zone.

In the electrodes and the GDL of a PEM fuel cell, the average pore size is larger than in the membrane. Water starts to freeze there first, because of the reduced freezing point depression in larger pores resulting in water drag from the membrane into the electrodes. When the fuel cell is heated up again, the conductivity rises due to melting water moving from the GDLs or electrodes into the membranes again. In the curve of Fig. 2 for stackW during F/T cycling (stack$W_{F/T}$), not all water returns to the membrane, and the conductivity after the F/T cycle of stack$W_{F/T}$ does not reach its initial value.

3.1.2. Distribution of water during F/T cycles and cold start-ups

The curve shape at low temperatures during the heating of stackW_{CS} is nearly the same as that during the cooling of stack$W_{F/T}$. When the hysteresis effect is included, the conductivity of stack$W_{F/T}$ lies between the two branches, and the conductivity of stack$W_{F/T}$ is slightly lower than that of stackW_{CS}. It is assumed that the membranes in stackW_{CS} reached the highest possible conductivity below 0 °C.

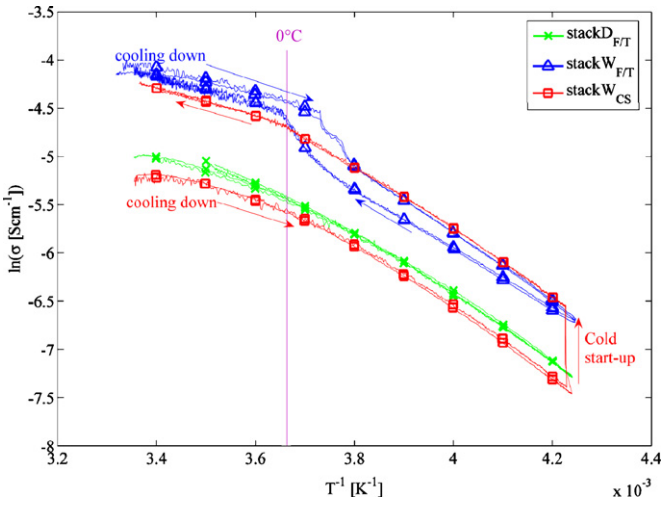

Fig. 2. Arrhenius plot of stack conductivity while cooling down and heating up during F/T cycles and cold start-ups. stack$W_{F/T}$: stackW during F/T cycling; stack$D_{F/T}$: stackD during F/T cycling; stackW_{CS}: stackW before and after a cold start-up. To demonstrate the good reproducibility of the experiments, two plots of each type are shown for each process.

Table 1
Activation energy above and below 0 °C

	E_A (kJ mol^{-1})					
	Cooling down @ $T>0$ °C	Cooling down @ $T<0$ °C	ΔE_A	Warming-up @ $T>0$ °C	Warming-up @ $T<0$ °C	ΔE_A
stackD	−17.00	−25.04	8.04	−18.60	−25.32	6.72
stackW	−11.39	−26.21	14.82	−12.47	−23.18	10.71
Cold start	−16.16	−26.81	10.68	−13.86	−26.58	12.72

The slopes were extracted in the temperature range between 0.1 °C (3.65×10^{-3} K^{-1}) and 8.7 °C (3.55×10^{-3} K^{-1}) as well as −13.3 °C (3.85×10^{-3} K^{-1}) and −19.8 °C (3.95×10^{-3} K^{-1}).

Throughout warming-up after cold start-ups, the membranes were fully humidified and no additional contact resistance reduced the conductivity. When stack operation is started under sub-zero conditions, the product water is first absorbed by the membranes. Once the membranes are fully humidified, the water cannot be absorbed by the ionomer and accumulates in the catalyst layer, where it freezes and finally causes a collapse of the cell voltages [9,17].

During each cold start-up series, the stack was started repeatedly in the galvanostatic mode under isothermal conditions (about 15 times). When the cell voltage dropped below 100 mV, operation was stopped. After the OCV had stabilized, the galvanostatic load was applied again. This procedure was repeated as long as the OCV stabilized above 0.3 V. By adopting this method, all membranes in the stack were expected to be fully humidified.

The reproducibility of the cold start-up experiments was very good and even for stackW$_{F/T}$, the conductivity below 0 °C was never distinctly higher than for stackW$_{CS}$ during warm up as shown in Fig. 2. Furthermore, when stackW$_{CS}$ was heated, the absence of a shift in conductivity around 0 °C indicates that ice did not reduce the contact resistance.

In contrast to stackW$_{CS}$ around 0 °C, a step change in conductivity is observable for stackW$_{F/T}$. This step does not result from residual water which freezes in the cell layer interface, causing an additional contact resistance, or from dehydration by frost heave. In those cases, the conductivity at −40 °C of stackW$_{F/T}$ would be distinctly lower than the conductivity of stackW$_{CS}$. Thus, the step in HFR must mainly be attributed to other causes. An explanation for this effect could be the Schröder paradox as described in Refs. [21,22]. The water content in Nafion© membranes can reach only $\lambda = 14$ when they are equilibrated in a water vapour atmosphere. In the presence of liquid water, the capillary pressure in electrodes is greater than 0 and therefore the water content in the membrane increases up to $\lambda = 22$.

Before freezing stackW$_{F/T}$, it was operated under normal conditions. The catalyst layers were partially flooded and the membranes were in contact with residual water, so the membrane channels were expanded ($\lambda > 14$) according to the model of Weber et al. If the residual water outside the membrane is freezes, the capillary pressure decreases and water drains out of the membrane and freezes also. This process lasts as long as the membrane channels collapse.

During the heating process, the phase transition from ice to liquid water results in an increase of the capillary pressure and the membrane channels expand again, resulting in a step-like increase in conductivity.

stackW$_{CS}$ does not show this step-like rise in conductivity. Due to the dry state of stackW before the cold start-ups, electrodes contain only a small portion of ice at −40 °C, located as a thin layer around the agglomerates. On melting, the liquid water spreads into the pores of electrodes and GDL, and the resulting capillary pressure is not high enough to cause a sudden change in conductivity.

3.1.3. Activation energies

Table 1 shows the activation energy from the three Arrhenius plots, which can be calculated from the slope of the Arrhenius curves in Fig. 2 [23].

Comparable differences between the activation energy above and below 0 °C (ΔE_A) were also reported by other groups [23,24]. Cappadonia et al. assume that the phase transition of water within the membrane is the reason for the change in activation energy [25]. ΔE_A for stackW, which was frozen in a wet state, is the highest because of its initial membrane water content. Below 0 °C, the activation energy seems to be independent of the water content, as also observed by Cappadonia et al. [25]. The activation energy of about 26 kJ mol^{-1} was also measured earlier in single-cell experiments [24].

3.2. Effects of sub-zero exposures on operational behaviour

The change of the steady-state voltage during galvanostatic operation and the HFR of stackD and stackW are shown in Figs. 3 and 4. Due to a test bench failure, cell 3 from stackW had

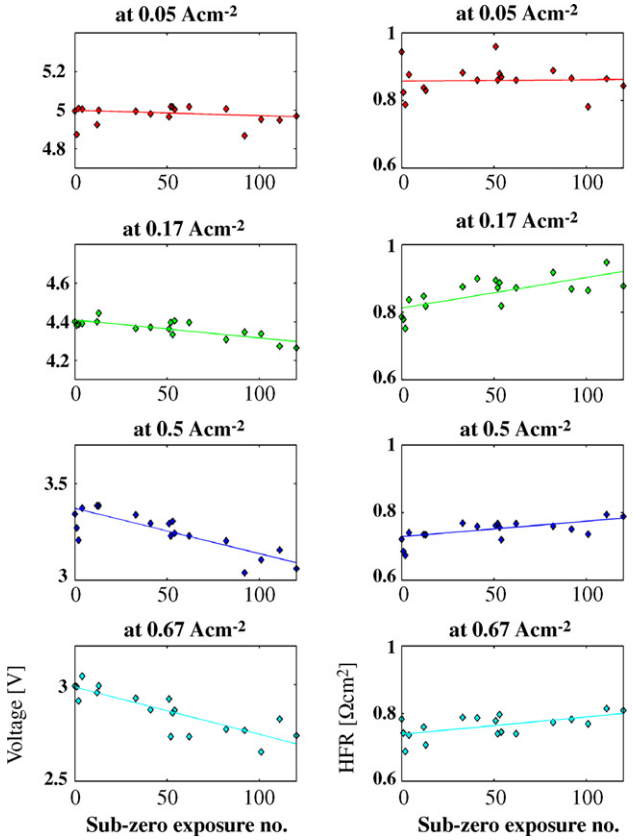

Fig. 3. Stack voltage and HFR in the galvanostatic operation mode of stackD during 110 sub-zero exposures.

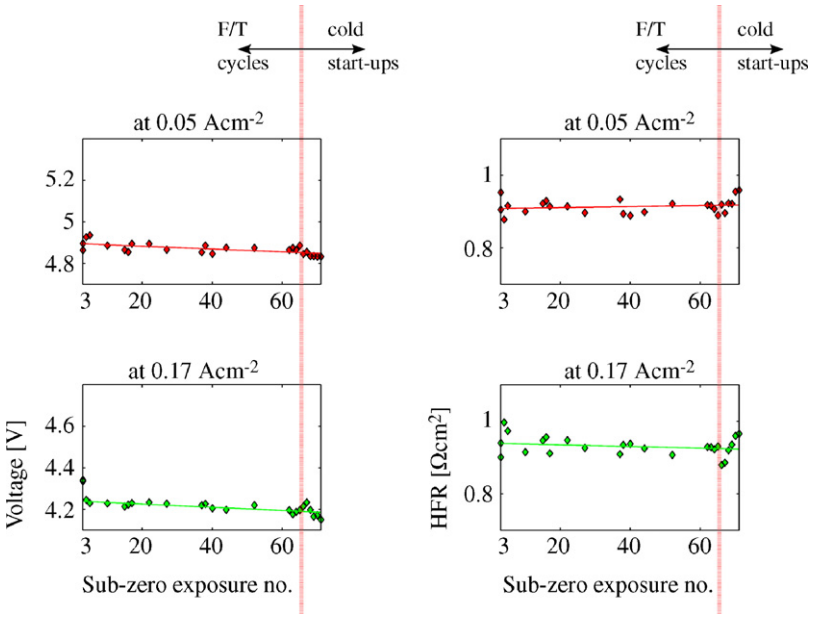

Fig. 4. Stack voltage and HFR in the galvanostatic operation mode of stackW during 71 sub-zero exposures.

to be replaced after F/T cycle #3 (measurement #6), so Fig. 4 shows measurements after the replacement only. Further measurements revealed that the other cells were not affected.

An increase in HFR can be observed for stackD which may result from a diminishing stack compression and additional drying effects (see Section 3.3). To reduce that effect, the compression of stackW was adjusted regularly, with the result that the HFR stayed constant.

At low current densities, stackW and stackD showed a similar but small decrease in performance. This confirms the results of other groups [8,5], where performance losses were mainly observed at high current densities, and is attributed to increasing mass transport limitations. After about five F/T cycles of stackW, the stack voltage at high current densities did not stabilize at steady state any more. To investigate this effect in more detail, the time-dependent voltages, temperatures and HFRs for a load change from 0.17 A cm^{-2} to 0.5 A cm^{-2} are shown in Fig. 5. After the repeated sub-zero exposure, a larger decrease in stack voltage of 1.2 V after switching to the higher current density can be observed before sub-zero exposure than after it (ΔV = 1.4 V). This indicates increased mass-transport limitations, which were already present at 0.17 A cm^{-2}. On switching to 0.5 A cm^{-2}, the drop in stack voltage is higher because mass transport limitations affected the cell performance more strongly at high current densities. Increasing mass transport limitations can be attributed to a change in pore size distribution in the electrode due to mechanical forces by the water to ice volumetric expansion. Hou et al. [5] and Wang et al. [7] examined the pore size distribution and found an increased total porosity, caused by F/T cycles in a wet state. Kong et al. found an optimized pore size distribution to reduce mass transport limitations at high current densities [26]. The larger the pore size, the higher the liquid water saturation within the electrodes at equal capillary pressure. Since the capillary pressure of water within the

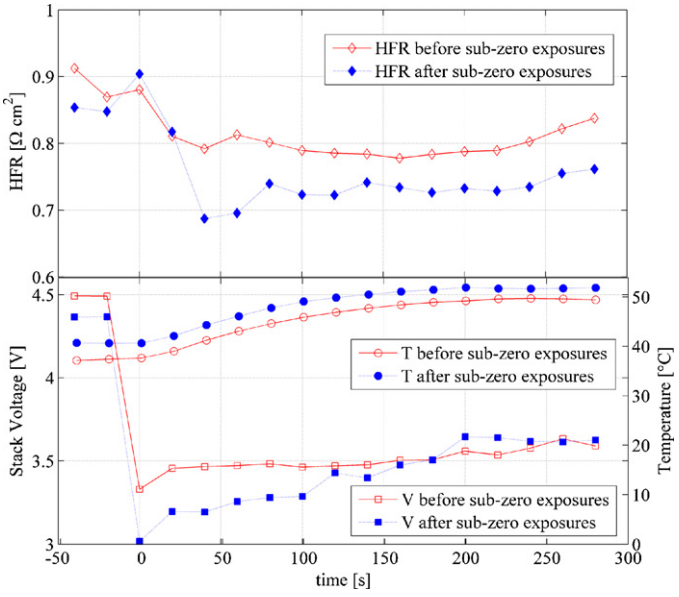

Fig. 5. HFR, voltage and temperature of stackW plotted over time after a load change from 0.17 A cm^{-2} to 0.5 A cm^{-2} before and after sub-zero exposure.

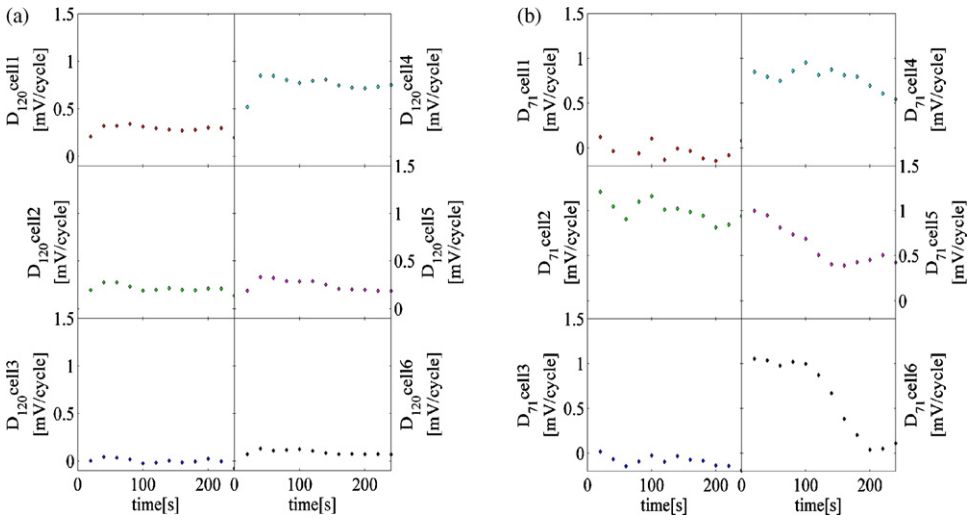

Fig. 6. Degradation rates of single-cell voltages of stackD (a) and stackW (b) over time after switching the current density for operation from 0.17 A cm^{-2} to 0.5 A cm^{-2}.

GDL and the electrodes is the same at the interface, liquid water saturation in the electrodes increases [27] when unchanged capillary pressure and saturation in the GDL are assumed. Due to the greater water saturation in the cathode electrode, diffusion of oxygen through the electrodes is reduced [27] and mass transport limitations are increased. Increased liquid water saturation in the electrodes after sub-zero exposure may also be the reason for the decreasing HFR at the higher current density.

Due to increased mass transport losses after sub-zero exposure, the temperature at a current density of 0.5 A cm^{-2} increases to 49 °C before sub-zero exposure and to 52 °C after sub-zero exposure. As residual water is removed from the electrode due to the higher water uptake capacity of reactant gases at higher temperatures, the HFR is increases. Thus, without the influence of increased mass transport limitations, the stack voltage increases to a level as high as the voltage before sub-zero exposure.

In order to ensure better comparability of the results, degradation rates were calculated as follows. In the experiment, the single cells were characterized after several sub-zero exposures, and a linear fit to the cell voltage versus the number of sub-zero exposures was extracted from the curve. The slope of the fitted curve after n sub-zero exposures was defined as the degradation rate D_n.

Fig. 6 shows the degradation rates of cell voltages of stackD (a) and stackW (b) over time after switching from 0.17 A cm^{-2} to 0.5 A cm^{-2}.

In Fig. 6, the average degradation rate of stackD (0.26 mV per sub-zero exposure) is lower than that of stackW (0.48 mV per sub-zero exposure). Furthermore, the time dependence of degradation

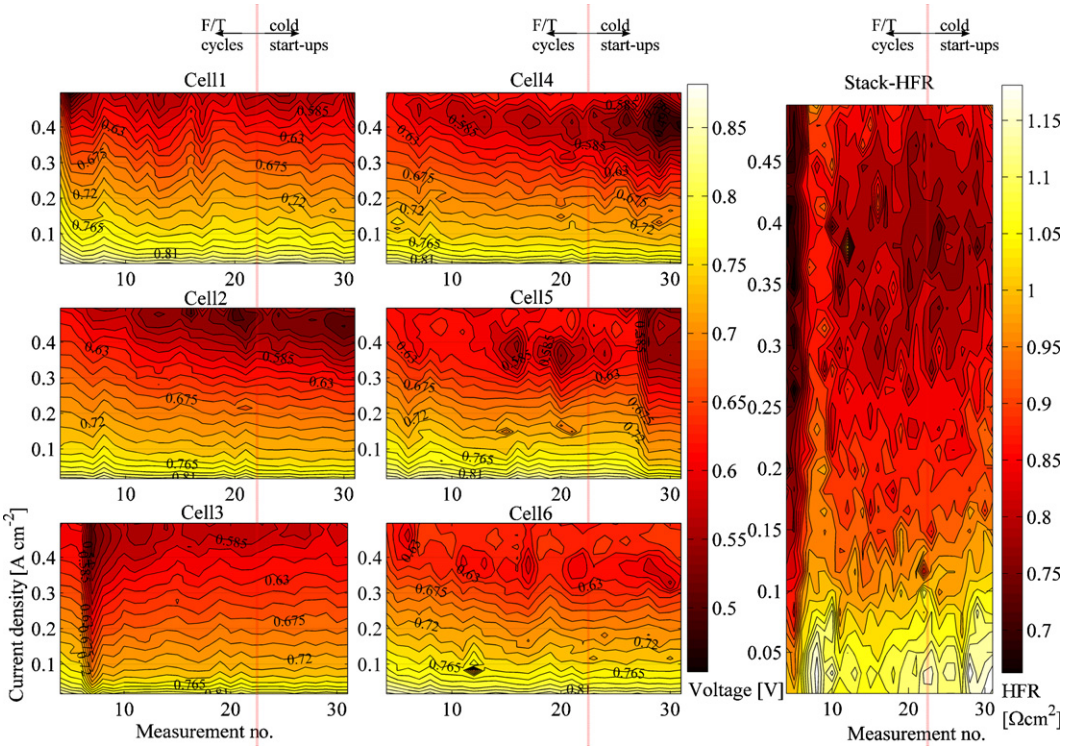

Fig. 7. Contour plot of the change in cell polarisation curves (left) and HFR (right) of stackW.

rates is much stronger for stackW than for stackD (note the different platinum loading of stackD and stackW). Especially cells 4, 5 and 6 in stackW seem to improve over time after switching to higher current density. In both stacks, the degradation rates exhibit a huge difference between the single cells. A correlation between the degradation rates of the single cells and their position in the stack is not obvious. Inhomogeneous conditions during drying or operation of the stack resulted in inhomogeneous conditions during sub-zero exposure and could be the reason for this huge variation of degradation rates.

In stackD, cells 3 and 6 seem not to degrade at all, while cell 4 shows an average degradation rate of 0.8 mV per sub-zero exposure.

In stackW, cells 1 and 3 show no performance degradation, while the average degradation rate of cells 2 and 4–6 is 0.75 mV per sub-zero exposure. In general, degradation rates are strongly time-dependent and are especially high directly after switching from 0.17 A cm^{-2} to 0.5 A cm^{-2} operation. Accordingly, the sub-zero exposure seems mainly to affect the extent of reversible effects (cell flooding). This shows that steady-state values at high current densities can hardly describe the degradation caused by the sub-zero exposure, since degradation describes the irreversible change of components. Besides that, after several sub-zero exposures, the voltages at higher current densities did not stabilize at all.

The change of the scanning polarisation curves and HFR of stackW throughout F/T and cold start-up experiments is visualized by interpolated contour plots in Fig. 7. Voltage is coded by colour and is plotted versus current density (y-axis) and the measurement number (x-axis). This way, all polarisation curves are positioned vertically adjacent in the contour plot and the space between is interpolated. Degradation is indicated by decreasing potential lines.

While the polarisation curves were recorded, the stack temperature increased from 26 °C at 0 A cm^{-2} to 57 °C at 0.5 A cm^{-2}. After measurement #6 (which corresponds to F/T cycle #3 of stackW), the MEAs and GDLs of cell 3 had to be replaced due to a test bench failure. As can be seen, this did not affect the performance of the other cells, but after being replaced, cell 3 did not show any performance degradation.

After measurement #27, cell 5 shows a drop in cell performance for no obvious reason. Because the single-cell OCV did not change, external leakage is the most likely reason for this.

During F/T cycling and cold start-up experiments, especially cell 4 showed an increasing distinct minimum of cell voltage at 0.4 A cm^{-2}, which is most likely caused by mass transport limitations due to cell flooding. At higher current densities, the higher temperatures caused a removal of the residual water, recognizable by the rising cell voltages and HFR (Fig. 7, right). The degradation rates of all cells except cells 3 and 1 decrease and the potential lines converge to a horizontal line with increasing number of sub-zero exposures. A difference in degradation behaviour between cold start-ups and F/T cycles cannot be observed. After 62 F/T cycles (measurement #22), the performance of all single cells does not even seem to be influenced by cold start-ups at all.

Fig. 8 shows the degradation rates of single-cell voltages at different current densities after 71 sub-zero exposures D_{71}. Obviously, the highest degradation rates are within current densities (0.4 A cm^{-2}) where cell flooding was the reason for a performance decrease in Fig. 7.

According to the degradation rates plotted in Fig. 6(b), cells 1 and 3 do not seem to degrade at all and cell 3 even seems to improve at high current densities. Cell 6 exhibits a distinct maximum which is attributed to cell flooding. At high current densities, when residual water was removed by gases at higher temperatures, the cell performance does not change throughout the sub-zero exposures ($D_{71} \approx 0$). This property of cell 6 has already been observed before,

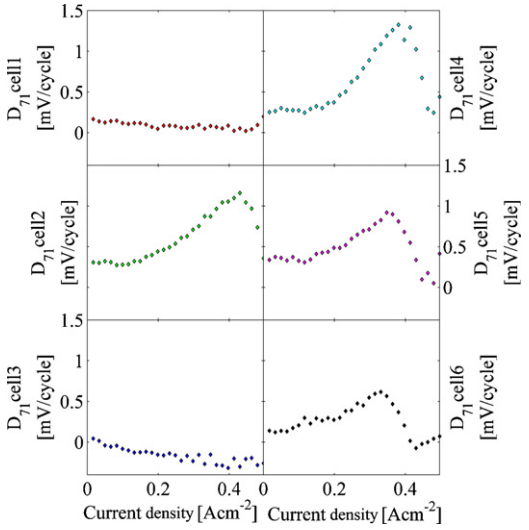

Fig. 8. Degradation rates at different current densities for stackW.

when the degradation rate declined to 0 mV per sub-zero exposure after being operated for 200 s at 0.5 A cm^{-2} (Fig. 6).

3.3. EIS analysis

EIS of the single cells in the stack were recorded in potentiostatic mode with a constant perturbation amplitude of 10 mV per single cell. As described in Section 3.2, the steady-state current density i_{st} decreases during repeated sub-zero exposure. Since the impedance Z strongly depends on the steady-state current density, it is difficult to evaluate EIS in the case of changing current. Jaouen and Lindbergh addressed the problem by defining the Tafel impedance Z_t [28]:

$$Z_t = \frac{-\tilde{E}}{\log(-\tilde{i})} = \frac{\tilde{E}}{\tilde{i}}(-i_{st}) = Z(-i_{st}).$$

Z_t is independent of the current density as long as mass transport limitations due to proton migration or oxygen diffusion are negligible. If mass transport losses are present, Z_t decreases with decreasing current.

In this paper $R_{D,T}$ is used for analysis of impedance spectra, which is defined as the diameter of the Tafel impedance Z_t, when plotted in a Nyquist diagram. $R_{D,T}$ is defined as the charge-transfer resistance of Z_t.

Figs. 9 and 10 show the Tafel charge-transfer resistance $R_{D,T}$ for stackD and stackW. For both stackW and stackD, the steady-state current density during EIS recording decreases from one sub-zero exposure to the next.

For stackD the Tafel charge-transfer resistance $R_{D,T}$ decreases as well (see Fig. 9) which might be addressed to loss of electrochemical surface area. According to Jaouen and Lindbergh [28] and Gerteisen et al. [29], a reduction of ECSA and exchange current density, respectively, does not affect the impedance but reduces the steady-state current density. Thus, Z_t decreases with ECSA loss.

Considering these interrelations one could conclude that ECSA should be reduced for stackD. This might result from repeated dry out before and insufficient re-humidification after F/T cycling of the catalyst layers before EIS recording. When the electrode is dry, the electrochemical three-phase zone is not as strong developed as in a well humidified state, and therefore ECSA could be reduced, which explains the decrease of $R_{D,T}$.

For stackW the Tafel charge-transfer resistance $R_{D,T}$ increases with repeated F/T cycles and decreasing i_{st} (see Fig. 10). Jaouen and

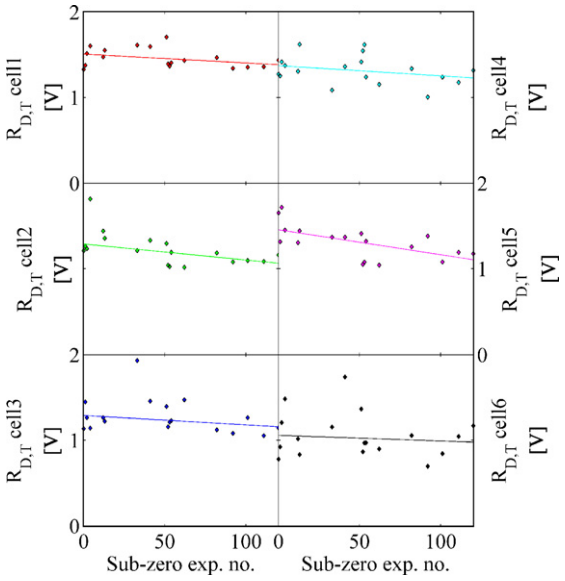

Fig. 9. Tafel charge-transfer resistance $R_{D,T}$ for all single cells in stackD.

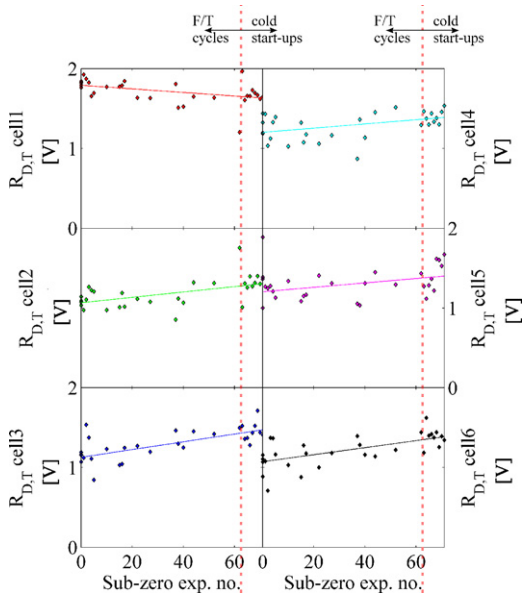

Fig. 10. Tafel charge-transfer resistance $R_{D,T}$ for all single cells in stackW.

Lindbergh explain such a behaviour with a reduced O_2-diffusion inside the electrode. By repeated F/T cycling, the morphology and the hydrophobic properties of the electrode are affected by ice formation [4–7,11–13]. As a result, the electrode has a stronger tendency for flooding and O_2-diffusion is limited more and more. Therefore the slope of the polarisation curve gets steeper.

While Z_t and $R_{D,T}$, respectively, increase in the experiments, the mass transport losses in the electrode must increase from each EIS analysis to the next.

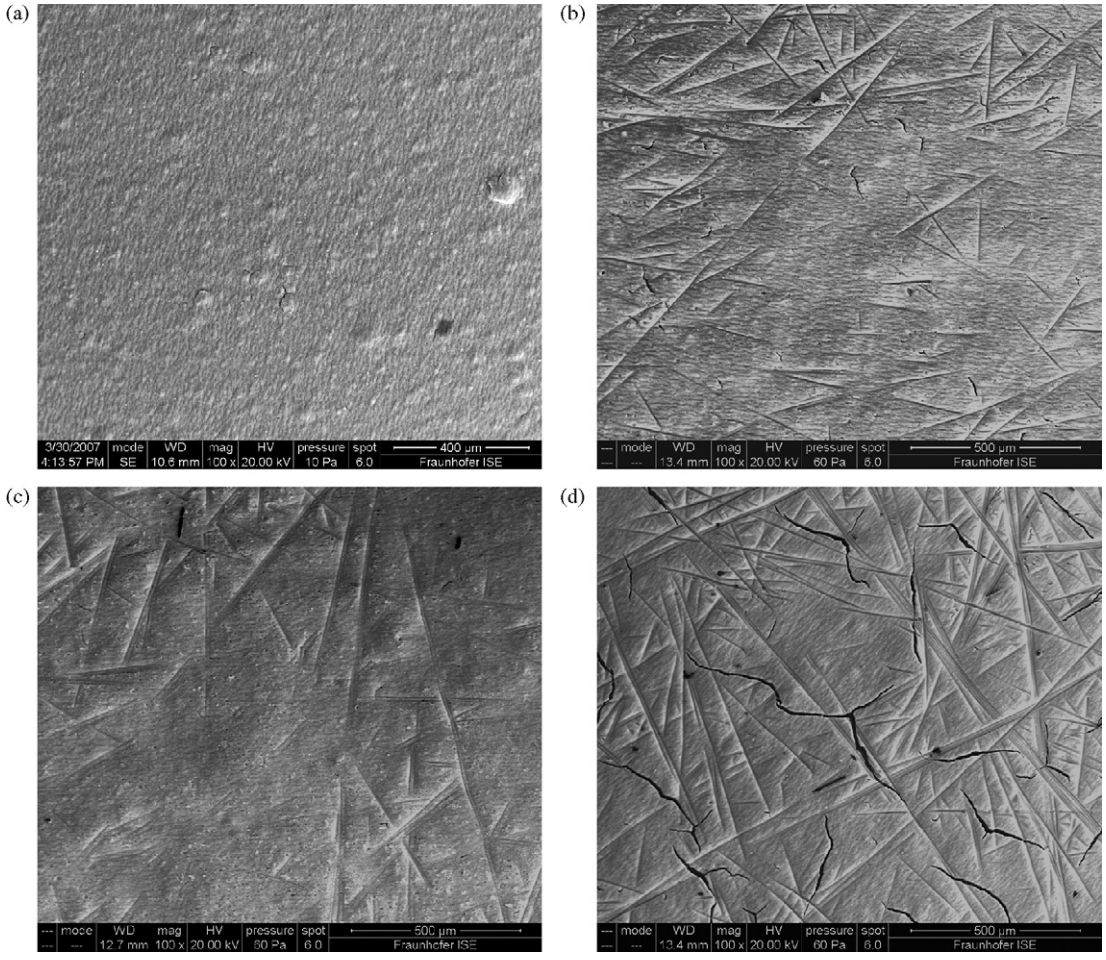

Fig. 11. SEM images of cathode electrode surface of new (a), stackD (b), stackW (c) and stackR (d) MEAs.

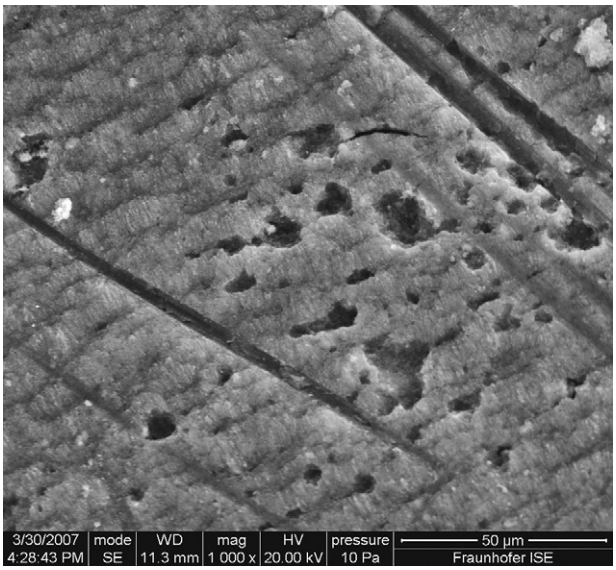

Fig. 12. Micro-cavities in stackW after F/T cycling.

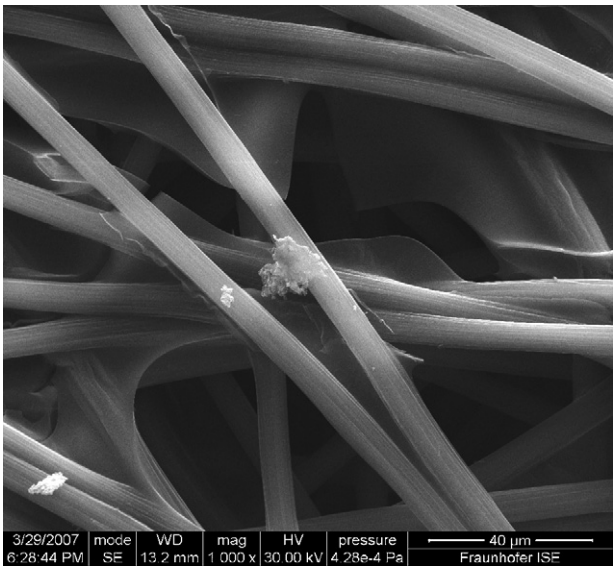

Fig. 13. GDL of stack D on the side facing the flow field.

The results of the EIS measurements of stackW are in good agreement with the results of the performance characterization in Section 3.2. Increased $R_{D,T}$ in Fig. 10 indicates increased mass transport losses for cells 2 and 4–6 which causes the high degradation rates in Figs. 6 and 8 and low voltage levels in Fig. 7. The hardly changed $R_{D,T}$ in Fig. 10 for cell 1 correlates with the unchanged cell performance (Figs. 6–8). Only the increasing $R_{D,T}$ of cell 3 (Fig. 10) is in contrast to the increasing cell voltage (Fig. 7) and negative degradation rates (Figs. 6(b) and 8) at high current densities, which is currently not understood.

3.3.1. Summary of EIS analyses

F/T cycling of PEM fuel cells could lead to increased mass transport losses in the electrodes. In contrast to dry frozen stacks, F/T cycling of wet frozen stacks results in reduced O_2-diffusion. Furthermore, insufficient re-humidification after F/T cycles can result in reduced electrode kinetics induced by less developed three-phase zones. Wet frozen PEM fuel stacks do not exhibit this behaviour, which might be partly reversible.

3.4. ESEM and ICP measurements

After both stacks had been operated for 90 h, they were disassembled and an ESEM was used to investigate the change in surface morphology of the MEAs and GDLs of both stacks. A third stack (stackR, with TGP-H-090 GDLs and the same MEAs as within stackD) was examined and served as a reference. It was operated for about 400 h and did not experience any sub-zero conditions.

In Fig. 11, typical images of the catalyst surface structure of a new MEA (a), a MEA from stackD (b), a MEA from stackW (c) and a MEA from the reference stack (d) are shown. All assembled MEAs exhibit imprints of the GDL fibres, but neither stackD nor stackW showed any dramatic structural change in the electrode surface as observed by Guo and Qi [4]. Though it had not been exposed to any F/T cycle, the reference stack was the only one to have distinct cracks on the surface, which were most likely formed by swelling/shrinking processes during normal MEA operation.

Unlike in the reference stack, the surface of the MEA electrodes of stackD and stackW showed micro cavities with diameters of about 10 µm as can be seen in Fig. 12.

Fig. 13 shows the surface of a cathode GDL of stackD which faced the flow field. Mukundan et al. reported fibre breaks in the GDL

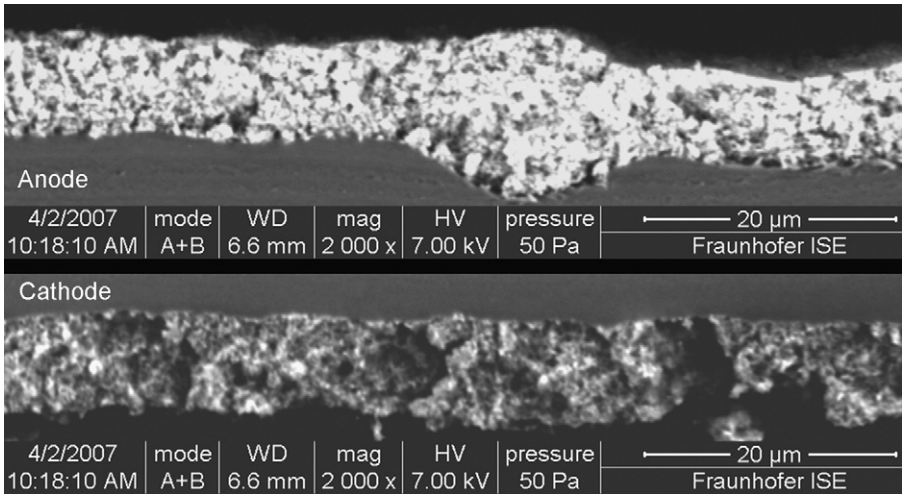

Fig. 14. Cross-section of MEA catalyst layers after 71 "wet" sub-zero exposures in stackW.

Table 2
Average changes in cross-section electrode surface areas (ΔX_{es}), compared to new MEAs

	stackD (%)		stackW (%)		stackR (%)	
	ΔX_{es}	RSTD	ΔX_{es}	RSTD	ΔX_{es}	RSTD
Anode	+3.6	10.9	−13.0	21.4	−15.7	13.6
Cathode	−9.4	10.1	−35.9	25.3	−28.2	23.6
Difference	13.0		22.9		12.5	

Relative standard deviations (RSTD) of 6 × 10 measurement points.

and binder damage [8], which could not be confirmed by Fig. 13. Examination of the GDL surfaces facing the MEA, revealed pieces of the electrode sticking to the GDL surface. It cannot be excluded that these pieces resulted from mechanical stress in the cell, causing the electrode to stick to the GDL surface when the stack was disassembled.

Particles were found on the GDL surfaces facing the flow field only for the electrode surfaces of the two stacks which were exposed to low temperatures (stackD and stackW) (Fig. 13). EDX measurements revealed that these particles came from the electrode, as indicated by their high platinum content. These particles detached from the electrode within the stack and moved through the GDL and were most likely formed during sub-zero exposure.

Cross-sections of MEAs of the frozen stacks, of the reference stack and of new MEAs were examined to analyze the effect of sub-zero exposure on membranes, electrodes and interfaces. It was obvious that cathodes of the "wet" frozen stackW were significantly damaged by the sub-zero exposure due to their higher porosity (Fig. 14). As reported by other groups [11–13,7], the membrane–electrode interface does not seem to be affected by in situ sub-zero exposure.

A mathematical algorithm for image analysis was used to quantify the decrease of electrode material by evaluating the ESEM images. The algorithm detects the contiguous bright regions separately for the anode and cathode sides in cross-section images and calculates a characteristic value (sum of detected pixels) for the cross-section images. Ten SEM images were evaluated for each cell of stackD, stackW and stackR as well as for two new MEAs. Table 2 shows the decrease in electrode surface area ΔX_{es} for all three stacks. ΔX_{es} is calculated as the average of 60 (6 × 10) deviations of values found for stack MEAs (A_i) relative to the values found for the new MEAs (A_{new}):

$$\Delta X_{es} = \frac{1}{60}\sum_{i=1}^{60}\frac{A_i - A_{new}}{A_{new}}$$

The relative standard deviation (RSTD) is given for the deviation of the electrode surface area from the average for all 60 electrodes.

All cross-sections showed significantly lower values for the cathode than for the anode electrode surface area. stackD exhibits just a slight decrease in cathode surface area while the anode surface area is not reduced at all.

Although the operating time of stackR was about five times higher than that of the two frozen stacks, the cathode ΔX_{es} for stackW is 27% higher than for the reference stack. Additionally, the decrease of the cathode surface area is 176% higher than the decrease of the anode surface area in stackW, while the decrease of the cathode surface area of stackR was only 80% higher than that of the anode surface area.

From this we conclude that the electrode surface areas already decrease during standard operation, especially for the cathode. F/T cycling in a "wet" stack status and cold start-ups accelerate the reduction of surface areas in cross-sections, especially on the cathode side.

Table 3
Average and standard deviation of the concentration of platinum 194 amu and 195 amu in condensed anode and cathode exhaust water of stackD and stackW

	Anode		Cathode	
	Average (ng l^{-1})	STD (ng l^{-1})	Average (ng l^{-1})	STD (ng l^{-1})
stackD	59	52	83	52
stackW	34	25	65	41

The concentration of platinum isotopes 194 amu and 195 amu in the product water of both stacks was examined by ICP-MS. Significant platinum concentrations were found, but neither the platinum concentration nor the absolute amount of platinum in the samples showed any correlation with sub-zero exposure. Table 3 shows that for stackD (frozen in a dry state) the platinum concentration was even higher than for stackW (frozen in a wet state). This may be caused by the slightly higher platinum concentration of the MEAs in stackD. Wet F/T cycling and cold start-ups did not result in a higher platinum concentration in the condensed water of the anode/cathode off-gas.

SEM top views of electrodes showed serious detachment of the electrode. Furthermore, particles were found on the GDL surfaces facing the flow fields. These particles detached from the electrode surface, migrated through the GDL and were taken up by the adjacent surface of the GDL. Other particles are expected to be carried out by the airflow. However, since particles with diameters larger than 5 μm are hard to detect by ICP, most of the particles in Figs. 12 and 13 (with diameters of about 15 μm) were most likely not detected. The high standard deviation of the measurements indicates that some of the particles were detected occasionally. As a result, no quantitative statement can be made, whether the amount of particles in the condensed water from the off-gas of stackW was higher than in stackD. In situ degradation of stackW was higher than that of stackD, but the platinum concentration was the highest for stackD. Most likely, the sub-zero exposures had little influence on the detected amount of platinum in the condensed water and the platinum dissolved from the electrodes and was washed during to standard operation of the fuel cell stacks.

3.5. Examination of hydrophobic properties of GDLs

Prior to contact angle measurements, the GDLs were sprayed with distilled water to visualize inhomogeneous hydrophobic properties of the GDL surface. No hydrophilic regions or flow field channel patterns could be observed as reported in our previous work [9], where additional micro-porous layers were used in cold start-up experiments. After drying the GDLs, the contact angle was determined.

stackD GDL surfaces showed even a slightly greater loss of hydrophobicity than those of stackW and the loss for the MEA-facing side of GDLs was slightly smaller than that of the other side (Table 4).

As described by Lee and Merida [10], the GDL surface was most likely not affected by the sub-zero exposure. Differences can be

Table 4
Comparison of average contact angles and standard deviations (STD) of GDL samples on the side facing the flow field (FF) and the MEA (MEA), respectively

	Anode				Cathode			
	Average (°)		STD (°)		Average (°)		STD (°)	
	FF	MEA	FF	MEA	FF	MEA	FF	MEA
stackD	126.1	130.4	4.4	3.0	131.6	131.8	2.2	1.9
stackW	135.3	136.4	2.0	1.4	134.3	136.9	1.1	1.3
New sample	Average: 136.5		STD: 0.8		32 measurement points			

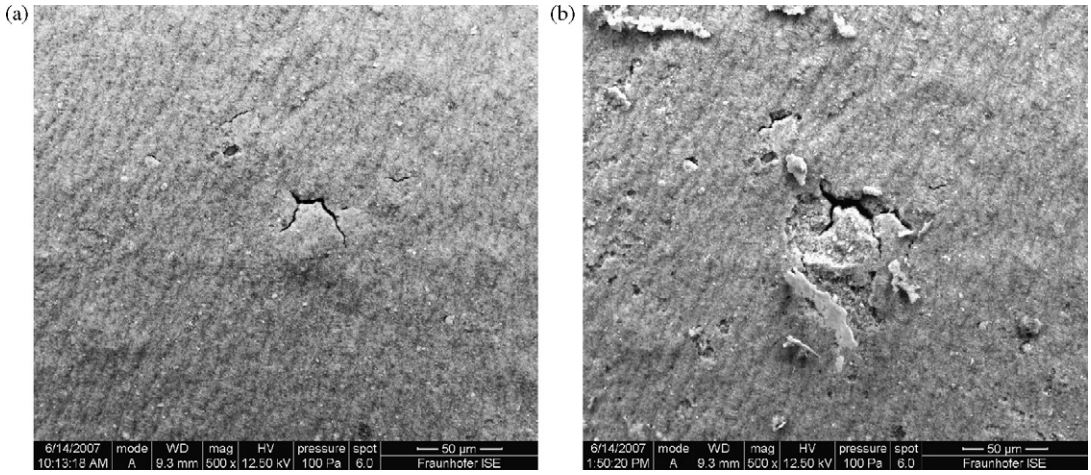

Fig. 15. Electrode surface of MEA before (a) and after (b) 10 F/T cycles ex situ in ESEM.

attributed to changes in the surface chemistry of fibres, PTFE loss, PTFE degradation or contaminants [10].

3.6. Ex situ F/T cycling of MEAs and GDLs in ESEM

Three spots of a new MEA electrode surface were examined before and after 10 ex situ F/T cycles from −20 °C to 0.5 °C in the ESEM. Distinct damage was found for all three spots. ESEM images of MEA samples in Fig. 15 before (a) and after (b) F/T cycles revealed the results caused by sub-zero exposure of the fuel cell stacks.

SEM images of MEAs from stackW (62 F/T cycles and 9 cold start-ups) do not show cracks but micro-holes and detachment of electrode pieces are visible (Fig. 12).

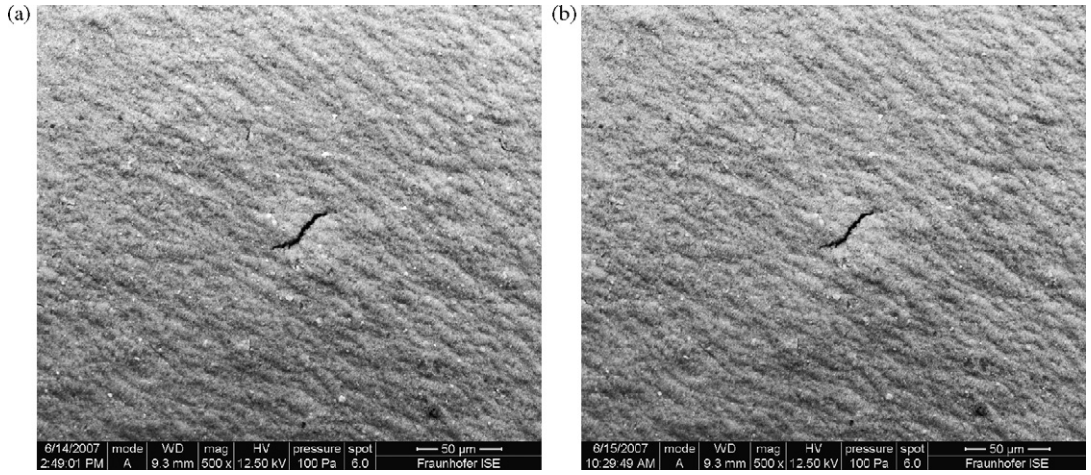

Fig. 16. Electrode surface of a MEA before (a) and after (b) 10 wet-dry cycles ex situ in ESEM.

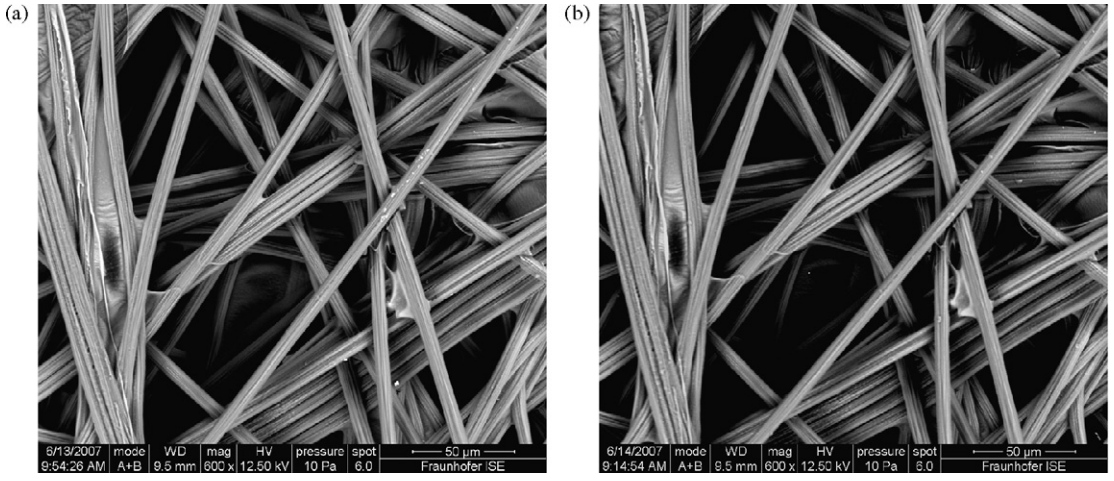

Fig. 17. Surface of GDL before (a) and after (b) 10 F/T cycles ex situ in ESEM.

Obviously, water in the electrode caused detachment when it experienced phase transitions. This effect was stronger ex situ, when the MEA is not compressed. During stack operation, the layers of the MEAs are compressed between GDLs, so, the mechanical bond is much stronger and detachment cannot occur to the same extent, as proven by analysis of the top view images after repeated sub-zero exposure of the stack (see Fig. 11).

To examine just the impact of membrane swelling due to water uptake on the MEA catalyst layer, 10 wet–dry cycles were conducted in the ESEM (without going below 0 °C). The temperature was stabilized at 0.5 °C while the atmospheric pressure was increased from 10 Pa to 700 Pa until the MEA surface was fully covered by condensing water. At this point, the pressure was decreased to 10 Pa again. Four spots on the MEA sample were examined before and after the wet–dry cycles and none showed any change in the electrode surface. Fig. 16 shows a spot before (a) and after (b) 10 wet–dry cycles. The crack in the catalyst layer did not expand. An additional examination was conducted at a constant pressure of 10 Pa and temperatures between −20 °C and 20 °C (10 cycles) to simulate dry F/T cycles. As expected, no change in the electrode surface was observed.

In Fig. 17, the GDL is shown before (a) and after (b) 10 F/T cycles. Neither fibre breakage nor any damage to the binder was observed here or at two further positions of the sample. This confirms the results of ex situ contact angle measurements and SEM imaging after stack F/T cycling and cold start-up experiments, where no influence of sub-zero exposure on GDLs has been found.

4. Conclusions

The impact of sub-zero conditions on stacks was investigated by freezing two fuel cell stacks, one in a dry and one in a wet state. During freeze–thaw cycling, it was found that the membrane water content below 0 °C can reach a maximum and that water drains out of the membrane and freezes in the catalyst layer. Step-like changes in the conductivity during the phase change of water can be explained by expanding/collapsing channels in the membrane (Schröder's paradox) and not by increasing contact resistance.

Repeated sub-zero exposure led only to slight performance degradation of a stack which was dried before freezing, mainly at high current densities.

The stack which was frozen in the wet state showed serious degradation which can be attributed to changes in water management resulting in poorer dynamic performance. After several sub-zero exposures, steady-state operation at higher current densities was not possible any more due to flooding effects.

Examination of the charge-transfer resistance revealed that mass transport limitations increased for the stack which was repeatedly frozen in a wet state. However, after 62 F/T cycles and 9 cold start-ups, this stack was still performing well and neither F/T cycling nor cold start-ups seem to have a dramatic influence on performance or charge-transfer resistance.

Cross-sections of the MEAs of both stacks showed an increase in porosity and a decrease in electrode surface area especially for the cathode electrode of the stack. This effect was increased when the stack was repeatedly frozen in a wet state. No cracks, but micro-cavities were found on the electrode surface of both stacks. Matching particles of the electrode were found, even on the surface of the GDLs, facing the flow field.

However, although ICP-MS measurements of the product water identified platinum in the condensed water of the exhaust gas of the anode and cathode, there was no correlation with F/T cycling or cold start-ups.

In both stacks, changes in the characteristics of single cells differ strongly from cell to cell, but a correlation between degradation and the cell position in the stack is hardly recognizable.

The observed characteristics lead to the following interpretation of the processes in a fuel cell during F/T cycling:

When a PEM fuel cell stack is cooled below 0 °C, water outside the membrane freezes and liquid water within the membrane drains out. As a result, only a little water freezes inside the membrane. The volume expansion during the phase transition of water within the electrode causes micro-cracks and cavities within the electrode and porosity increases. However, the compression of the MEAs and GDLs in an assembled stack prevents more serious crack-building and detachment of the electrodes. Only a few particles detach, move through the GDL and are transported out by the exhaust gas. During operation of the stack, the increased porosity leads to higher water saturation within the electrodes and the mass transport also becomes more limited. After disassembly of the stack, catalyst particles quarried out of the electrode due to ice formation are removed from the electrode surface.

In contrast to several results found in the literature, our work shows that degradation in PEM fuel cells at sub-zero conditions seems to be highly dependent on cell components, freezing conditions and characterization methods, which are often described incompletely. To avoid degradation at low temperatures, water has to be removed before freezing or the PEM fuel cell components have to be redesigned with greater material flexibility to allow volume expansion at the phase transition of liquid water to ice.

References

[1] A. Pesaran, G.H. Kim, J. Gonder, Fuel Cell Durability Workshop, Washington, DC, 2005, p. 205.
[2] M. Oszcipok, M. Zedda, J. Hesselmann, M. Huppmann, M. Wodrich, M. Junghardt, C. Hebling, J. Power Sources 157 (2006) 666–673.
[3] R.C. McDonald, C.K. Mittelsteadt, E.L. Thompson, Fuel Cells 4 (2004) 208.
[4] Q. Guo, Z. Qi, J. Power Sources 160 (2006) 1269–1274.
[5] J. Hou, H. Yu, S. Zhang, S. Sun, H. Wang, B. Yi, P. Ming, J. Power Sources 162 (2006) 513–520.
[6] M. Oszcipok, M. Zedda, D. Riemann, D. Geckeler, J. Power Sources 154 (2006) 404–411.
[7] H. Wang, J. Hou, H. Yu, S. Sun, J. Power Sources 165 (2007) 287–292.
[8] R. Mukundan, Y.S. Kim, F. Garzon, B. Piovar, Sub-freezing Fuel Cell Effects; DOE Hydrogen Program 2006 Annual Progress Report, V.G. 17, 2006.
[9] M. Oszcipok, D. Riemann, U. Kronenwett, M. Kreideweis, M. Zedda, J. Power Sources 145 (2005) 407–415.
[10] C. Lee, W. Merida, J. Power Sources 164 (2006) 141–153.
[11] S. Kim, M. Mench, J. Power Sources 174 (2007) 206–220.
[12] E.A. Cho, J.J. Ko, H.Y. Ha, S.A. Hong, K.Y. Lee, T.W. Lim, I.H. Oh, J. Electrochem. Soc. 150 (2003) A1667–A1670.
[13] E.A. Cho, J.J. Ko, H.Y. Ha, S.A. Hong, K.Y. Lee, T.W. Lim, I.H. Oh, J. Electrochem. Soc. 151 (2004) A661–A665.
[14] General Motors Corporation, Detroit MI (US), Freeze-protecting a Fuel Cell by Vacuum Drying, US Patent, 1999.
[15] Energy Partners, L.C. FL 33407 (US), Freeze Tolerant Fuel Cell System and Method, Patent, 1999.
[16] British Columbia V5J5j9 (CA), Methods for Improving the Cold Starting Capability of an Electrochemical Fuel Cell Patent, Ballard Power Systems Inc., Burnaby, 2000.
[17] S. Ge, C.Y. Wang, Electrochim. Acta 52 (2007) 4825–4835.
[18] R. Bradean, H. Haas, A. Desousa, R. Rahmani, AIChE 2005 Annual Meeting, T1, 322c, 2005.
[19] A. Hermansson, W.S. Guthrie, Cold Regions Sci. Technol. 43 (2005) 128–139.
[20] S. He, M.M. Mench, J. Electrochem. Soc. 153 (2006) A1724–A1731.
[21] T.E. Springer, T.A. Zawodzinski, S. Gottesfeld, J. Electrochem. Soc. 138 (1991) 2334–2342.
[22] A.Z. Weber, J. Newman, J. Electrochem. Soc. 150 (2003) A1008–A1015.
[23] A.M. Affoune, A. Yamada, M. Umeda, J. Power Sources 148 (2005) 9–17.
[24] M. Oszcipok, A. Hakenjos, D. Riemann, C. Hebling, Fuel Cells 7 (2007) 135–141.
[25] M. Cappadonia, J.W. Erning, S.M. Saberi Niaki, U. Stimming, Solid State Ionics 77 (1995) 65–69.
[26] C.S. Kong, D.Y. Kim, H.K. Lee, Y.G. Shul, T.H. Lee, J. Power Sources 108 (2002) 185–191.
[27] E.C. Kumbur, K.V. Sharp, M.M. Mench, J. Power Sources 168 (2007) 356–368.
[28] F. Jaouen, G. Lindbergh, J. Electrochem. Soc. 150 (2003) A1699–A1710.
[29] D. Gerteisen, A. Hakenjos, J.O. Schumacher, J. Power Sources 173 (2007) 346–356.